

Enhanced Spatiotemporal Prediction Using Physical-guided And Frequency-enhanced Recurrent Neural Networks

Xuanle Zhao, Yue Sun, Tielin Zhang and Bo Xu

Abstract—Spatiotemporal prediction plays an important role in solving natural problems and processing video frames, especially in weather forecasting and human action recognition. Recent advances attempt to incorporate prior physical knowledge into the deep learning framework to estimate the unknown governing partial differential equations (PDEs), which have shown promising results in spatiotemporal prediction tasks. However, previous approaches only restrict neural network architectures or loss functions to acquire physical or PDE features, which decreases the representative capacity of a neural network. Meanwhile, the updating process of the physical state cannot be effectively estimated. To solve the above mentioned problems, this paper proposes a physical-guided neural network, which utilizes the frequency-enhanced Fourier module and moment loss to strengthen the model’s ability to estimate the spatiotemporal dynamics. Furthermore, we propose an adaptive second-order Runge-Kutta method with physical constraints to model the physical states more precisely. We evaluate our model on both spatiotemporal and video prediction tasks. The experimental results show that our model outperforms state-of-the-art methods and performs best in several datasets, with a much smaller parameter count.

Index Terms—Physical-inspired Neural Networks, Physical-guided Update, Spatiotemporal Prediction, Video Prediction

I. INTRODUCTION

IN recent years, data-driven spatiotemporal prediction has attracted researchers’ attention in the field of deep learning, due to its ability to simulate complex dynamics and its widespread application in many challenging tasks, such as traffic flow prediction [1], human behavior estimation [2], and weather forecasting [3].

Data-driven deep learning algorithms usually select neural networks using convolutional and recurrent architectures to generate spatial and temporal features, respectively, such as,

Xuanle Zhao, Tielin Zhang are with the Laboratory of Cognition and Decision Intelligence for Complex Systems, Institute of Automation, Chinese Academy of Sciences (CASIA), Beijing 100190, China, and also with the School of Artificial Intelligence, University of Chinese Academy of Sciences (UCAS), Beijing 100049, China. (e-mail: zhaoxuanle2022@ia.ac.cn and tielin.zhang@ia.ac.cn).

Yue Sun is with the Laboratory of Cognition and Decision Intelligence for Complex Systems, Institute of Automation, Chinese Academy of Sciences (CASIA), Beijing 100190, China. (e-mail: yue.sun@ia.ac.cn)

Bo Xu is with CASIA, UCAS, and the Center for Excellence in Brain Science and Intelligence Technology, Chinese Academy of Sciences, Shanghai 200031, China. (xubo@ia.ac.cn).

The corresponding author is Tielin Zhang (tielin.zhang@ia.ac.cn)

This work was supported in part by the Strategic Priority Research Program of the Chinese Academy of Sciences, in part by the Shanghai Municipal Science and Technology Major Project and in part by the Youth Innovation Promotion Association of CAS.

including but not limited to, the convolutional neural networks (CNN) [4], multi-layer perceptions (MLPs), recurrent neural networks (RNN) [5], and transformers [6], and as a result, to improve spatiotemporal prediction accuracy. SimVP and MetaVP [4] utilize revised UNet (i.e., IncepUNet) and transformers (i.e., MetaFormer) to directly learn input-output sequential mapping without explicitly modeling temporal dependencies. Other transformer-based methods calculate spatiotemporal dependencies using natural attention mechanisms in both spatial and temporal manners, such as Swin Transformer [6] and Poolformer [7]. FNO [8] is inspired by conventional Green’s function and utilizes Fourier transformation to learn the mapping directly in the frequency domain. As a comparison, the recurrent-based methods can leverage well their distinct advantages in modeling sequential data, which as a result, can make them capture spatiotemporal representation intuitively. The ConvLSTM [9] combines spatial convolution and temporal recurrent connections by replacing the original linear operation of LSTM with convolutional modules. The E3D-LSTM [10] and CrevNet [11] run further by incorporating more complex 3D convolutions into LSTM modules, and similar modifications, such as replacing internal structures of the recurrent networks, have also been proposed in PredRNN [12]–[14] and PredNet [15].

However, it has been a generally accepted viewpoint, that the purely data-driven approach will encounter challenges in relatively small data size and noise perturbations, and result in non-smooth dynamic prediction. Some physics-informed neural networks have been proposed under these requirements, e.g., PhyDNet [16] incorporates some physical laws as regularization terms into the loss function, which to some extent, contributes to the feature modeling of underlying dynamics in spatiotemporal prediction tasks. The prior physical knowledge here is usually represented with the partial differential equations (PDEs) first (i.e., defining as the format of $\frac{du}{dt} = f(u)$), and then reformed as the format of $\frac{du}{dt} - f(u) = 0$ and added directly to the loss function as learning regularization. Many similar works [16], [17] has also been proposed to solve tasks in specific domains, such as precipitation [18] and weather forecasting [19].

Hence, it is obvious that both network architectures and physical PDEs can work as physical constrains (or knowledge) to further improve pure data-driven neural networks. Here, in this paper, we hold a similar view point with PhyDNet, whereby the integration of data-driven and physics-informed approaches are helpful in improving spatiotemporal prediction

accuracy.

The contributions of this work are summarized as follows:

- Inspired by recent transformer and FNO approaches, two main information pathways are incorporated into neural network architectures, including the Fourier-block-based pathway for spatial information processing, along with another transformer-LSTM-based pathway for temporal information processing.
- An adaptive second-order Runge-Kutta module (ARKM) is designed to make physical state estimation, after receiving two-pathway spatiotemporal information. The ARKM module contains an adaptive gate mechanism and PDE-guided convolution, along with a congruent moment loss in the total loss function.
- A high-frequency-dominated H1 loss is used to capture the high-frequency feature, which are usually omitted in PDE-informed neural networks, to well represent dynamic boundaries. Furthermore, the frequency domain H1 loss is combined with MSE loss and aforementioned moment loss, to force the network to learn spatial frequencies and temporal derivatives.
- The proposed algorithm is then tested in benchmark spatiotemporal prediction tasks, including vanilla PDE calculation and prediction (i.e., Navier-Stoke equation), and some typical machine-learning predicton paradigms, such as moving MNIST (i.e., dynamic handwritten digits), TaxiBJ (i.e., taxi trajectory prediction), KTH (human actions prediction), SEVIR (radar-based measurements of vertically integrated liquid), 2015-2018 weather prediction. Compared to some other state-of-the-art algorithms, our algorithm can achieve superior performance (i.e., lower error rate).

II. BACKGROUND AND RELATED WORKS

Our work shares common ground with several lines of research, and we will briefly cover the background and related works in this section.

A. Spatiotemporal Prediction Methods

Generally, the spatiotemporal prediction methods could be roughly divided into recurrent-based and recurrent-free methods. Recurrent-based models previously received more attention in prediction tasks since their ability to model sequence data. ConvLSTM [9] modifies the standard LSTM cell with convolution operations to model temporal dependencies. PredRNN [12] utilizes the vanilla ConvLSTM modules to directly model spatial and temporal variations simultaneously. PhyDNet [16] explicitly disentangles the hidden states into physical and residual spaces and utilizes convolution recurrent cells governed by PDEs to learn the physical representation. MAU [5] proposes a motion-aware unit and attention mechanism to capture temporal motion information. SwinLSTM [20] proposes a new recurrent cell that integrates Swin Transformer blocks and vanilla LSTMs. These methods have achieved superior performance in spatiotemporal prediction.

Recurrent-free methods could be further divided into CNN-based, Transformer-based, and physics-based methods. Previous CNN-based methods utilize 3D convolutions to learn

the temporal dependencies. SimVP [4] utilizes stacked inception modules to build spatial and temporal dependencies and directly map the previous and future frames. Transformer-based methods introduce Vision Transformers to model latent dynamics. Video Swin Transformer [6] builds on Swin Transformer to model 3D representations. TimeSformer [21] and ViViT [22] apply temporal and spatial attention to learn space-time dependencies. Recently, physics-based methods have received much more attention. FNO [8] directly learns mappings in the frequency domain and shows zero-shot ability in solving PDEs. Inspired by FNO, several works [23]–[25] have attempted to utilize the frequency domain to learn input and output mappings for simulating dynamic systems.

B. Physics-Informed Neural Network

Various deep learning frameworks have attempted to leverage the integration of physical knowledge, such as PDEs, to enhance their performance and capabilities. Categories of incorporating PDEs into the deep learning framework could be divided into two categories. Firstly, the underlying PDEs could be previously known as prior expert knowledge when solving specific domain problems, such as weather and turbulent flow. In this way, approaches like ClimODE [19] and NowcastNet [18] directly utilize convection equations for modeling correction and iteration.

Secondly, when solving general tasks without knowing the governing PDEs in advance, neural networks always approximate the governing PDEs in a data-driven way to incorporate the physical knowledge. For example, PDE-Net [26] utilizes convolutions with predefined forms to approximate the partial derivatives of the underlying PDEs to form a board class of PDEs. PhyDNet [16] disentangles the hidden space into physical space and residual spaces and utilizes moment loss to constrain the convolutions to approximate partial derivates of physical spaces. Earthfarseer [23] employs global Fourier-based transformers to extract global spatial information. PDE-STD [17] disentangles the spatiotemporal prediction into spatial and temporal representations to predict future observations precisely.

It is worth noting that many deep learning methods integrate other types of physical knowledge. Fourier neural operator (FNO) [8] draws inspiration from the conventional Green's function method and utilizes the Fast Fourier Transform (FFT) to optimize the kernel in the frequency domain. Inspired by FNO, Fourier-based methods have been proposed in various domains, including computer vision and time series forecasting. AFNO [27] leverages kernel in the Fourier domain as a token mixer within the transformer. FEDformer [28] utilizes sparse basis elements within the Fourier frequency domain to create a frequency-enhanced Transformer model. Meanwhile, GFNet [29] employs the element-wise multiplication of learnable global filters with features in the frequency domain to enhance the performance in image classification and transfer learning tasks.

Other approaches like Neural ordinary differential equations (NODE) [30] and Physical-informed neural networks (PINN) [31] also draw inspiration from conventional physical methods

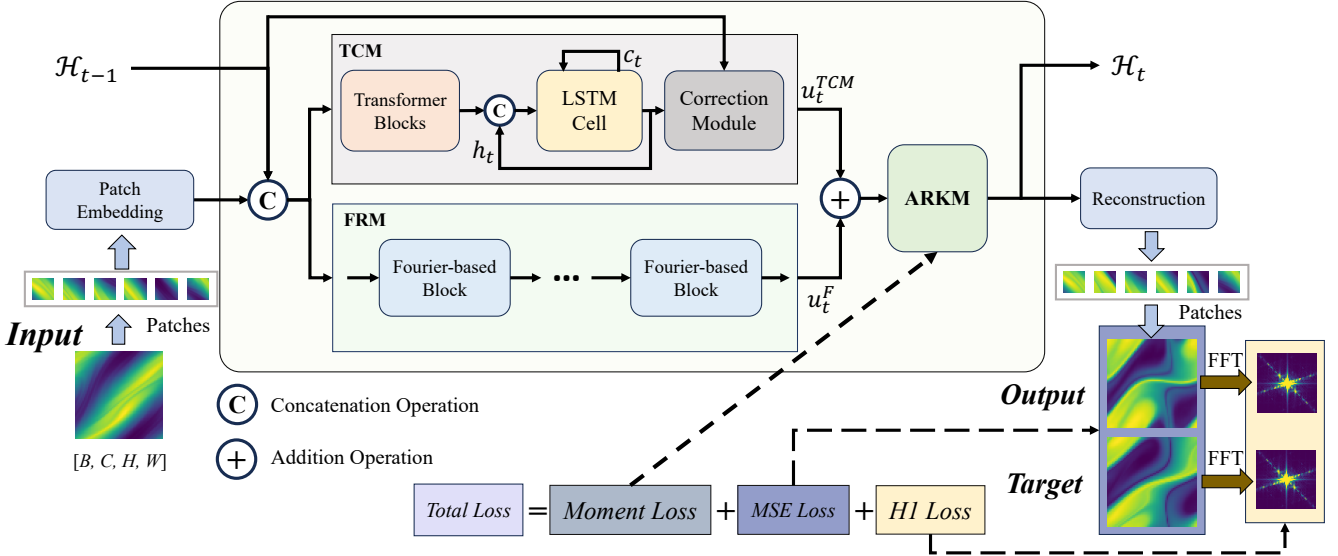


Fig. 1: The overall network architecture. The input frame is first embedded into patches. Then the previous hidden state and patches are concatenated and processed in TCM and FRM in parallel to output u_t^{TCM} and u_t^F . Finally, the representations are added and utilized in the ARKM for updating.

and show significant enhancement in designing the deep learning framework in various domains [32], [33].

III. METHODS

As depicted in Figure 1, our model compromises three components into a recurrent cell: the **Transformer-based Correction Module (TCM)** to model the general spatial dependency, the **Fourier-based Residual Module (FRM)** to learn physical representation and the **Adaptive second-order Runge-Kutta Module (ARKM)** for physical state estimation and iteration. The MSE loss, H1 loss, and moment loss make up the training loss function for the loss function.

A. Problem Preliminaries

In spatiotemporal prediction tasks, the model takes a sequence of past frames $\{x_1, \dots, x_T\}$ as input, where $x_t \in \mathcal{R}^{C \times H \times W}$ is the observation at timestep t . C , H , and W are the number of channels, height, and weight of the input frames. T is the input sequence length. The model aims to predict the future sequence $\{\hat{x}_{T+1}, \dots, \hat{x}_{T+T'}\}$ by minimizing the difference between the predicted frames and the true frames, where \hat{x}_t denotes the model prediction at timestep t and T' is the forecasting horizon. Specifically, as our model is trained recurrently, it takes the current frame x_t as the input and predicts the next frame \hat{x}_{t+1} . When inferencing the future sequence, the model takes the predicted frame as the input of the next step.

B. Model Architecture

Figure 1 shows the overall architecture of our model. Inspired by recent works, which assume that the latent space could be disentangled, our model attempted to leverage two parallel branches to model the latent spaces.

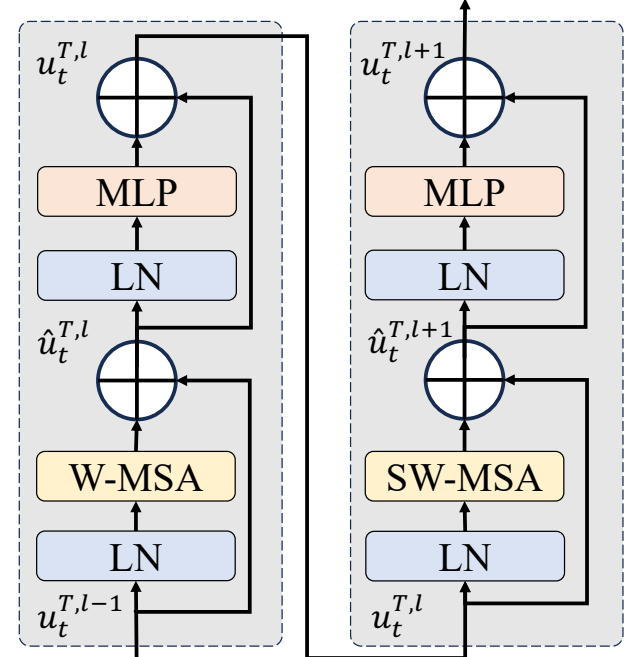


Fig. 2: The detailed structure of the Swin Transformer Block.

Specifically, given the input frame at the current time x_t , our model first embeds x_t into u_t by patch embedding. Then two parallel branches are used to represent the latent space. Our model uses transformer blocks and LSTM cells to extract general spatial features and correct hidden spaces respectively, and utilizes Fourier blocks to enhance the spatial dependencies in a physically guided way. Then, the outputs are added and updated using the adaptive Runge-Kutta module. The overall procedure could be denoted as:

$$\begin{aligned}
u_t^T &= \text{Transformer Blocks}((u_t; \mathcal{H}_{t-1})) \\
u_t^{TC} &= \text{LSTMCell}(u_t^T, h_t, c_t) \\
u_t^{TCM} &= \text{Correction Module}(u_t^{TC}, \mathcal{H}_{t-1}) \\
u_t^F &= \text{FRM}((u_t; \mathcal{H}_{t-1})) \\
\mathcal{H}_t &= \text{ARKM}(u_t^F + u_t^{TCM}),
\end{aligned} \tag{1}$$

where $(\cdot; \cdot)$ denote the concatenation operation. Finally, the updated hidden states \mathcal{H}_t are reconstructed to the prediction \hat{x}_t .

Transformer-based Correction Module (TCM). The global multi-head self-attention (MHSA) mechanism implemented in the Vision Transformer calculates the correlation among all the tokens, which improves the ability to represent spatial correlations. Swin Transformer proposes a window-based multi-head self-attention (W-WHSA) and shifted-window-based multi-head self-attention (SW-WHSA) to mitigate computational expenses and enhance modeling performance. The equations are listed in Equation (2) and $(u_t; \mathcal{H}_{t-1})$ is denoted as $u_t^{T,0}$.

$$\begin{aligned}
\hat{u}_t^{T,l} &= \text{W-MSA}(\text{LN}(u_t^{T,l-1})) + u_t^{T,l-1} \\
u_t^{T,l} &= \text{MLP}(\text{LN}(\hat{u}_t^{T,l})) + \hat{u}_t^{T,l} \\
\hat{u}_t^{T,l+1} &= \text{SW-MSA}(\text{LN}(u_t^{T,l})) + u_t^{T,l} \\
u_t^{T,l+1} &= \text{MLP}(\text{LN}(\hat{u}_t^{T,l+1})) + \hat{u}_t^{T,l+1},
\end{aligned} \tag{2}$$

The structure of the Swin Transformer block is based on the W-MHSA and SW-MHSA with two LayerNorm (LN) layers and a two-layer MLP with GLEU non-linearity. A LayerNorm layer and a residual connection are applied before and after each attention module and MLP module, respectively.

While Swin transformer blocks are utilized for extracting spatial correlations, the transient variant at each time step is not solely dependent on spatial context but also exhibits significant temporal coherence. To model the temporal coherence, we adopted an LSTM cell to learn the transient variation.

$$\begin{aligned}
i_t &= \sigma(W_{xi} * u_t^T + W_{hi} * h_{t-1} + b_i) \\
f_t &= \sigma(W_{xf} * u_t^T + W_{hf} * h_{t-1} + b_f) \\
o_t &= \sigma(W_{xo} * u_t^T + W_{ho} * h_{t-1} + b_o) \\
c_t &= f_t \odot c_{t-1} + i_t \odot \tanh(W_{xc} * u_t^T + W_{hc} * h_{t-1} + b_c) \\
h_t &= o_t \odot \tanh(c_t) \\
u_t^{TC} &= \text{MLP}(h_t),
\end{aligned} \tag{3}$$

where σ denotes the sigmoid function, W are convolutions with 1×1 kernel and b are the bias. $*$ and \odot are the convolution operator and the Hadamard product (element-wise multiplication) respectively.

Finally, the hidden states are corrected according to the input feature of the current time.

$$\begin{aligned}
u_t^{TCM} &= (1 - \mathcal{K}_t) \odot \mathcal{H}_{t-1} + \mathcal{K}_t \odot u_t^{TC} \\
&= \mathcal{H}_{t-1} + \mathcal{K}_t \odot (u_t^{TC} - \mathcal{H}_{t-1})
\end{aligned} \tag{4}$$

where $\mathcal{K}_t = \sigma(u_t^{TC})$ is the gating factor that balances the

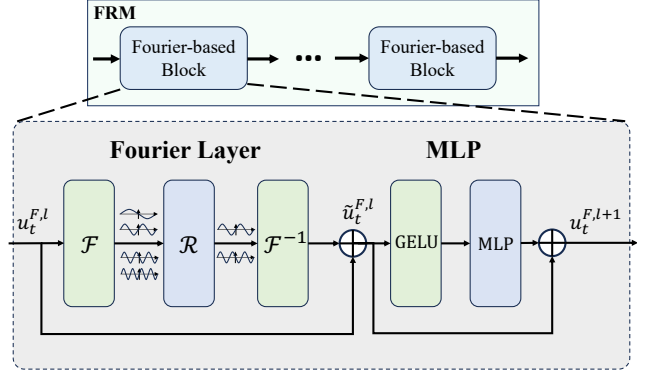


Fig. 3: The detailed structure of the Fourier-based residual block. In each block, the Fourier layer and MLP are computed serially.

predicted and previous hidden state.

Fourier-based Residual Module (FRM). This module aims to enhance the features learned by the transformer-based correction module in a physically guided data-driven way. The Fourier block is composed of the Fourier layer and MLP. The Fourier layer utilizes Fast Fourier transformation (FFT) and inverse Fast Fourier transformation (IFFT) with learnable kernels in the frequency domain to model the mapping function directly in the Fourier domain. In each Fourier block, 2D FFT \mathcal{F} is first applied to the input tokens

$$\mathcal{Z}_t^l(u, v) = \sum_{x=0}^{h-1} \sum_{y=0}^{w-1} u_t^l(x, y) e^{-2\pi i (\frac{u}{h}x + \frac{v}{w}y)}. \tag{5}$$

where $u_t^l(x, y)$ denotes the input of the l th Fourier block. Then, a kernel \mathcal{R}_ϕ parameterized by ϕ with real and imaginary parts is trained to multiply with $\mathcal{Z}_t^l(u, v)$ to compute in the Fourier domain.

$$\tilde{\mathcal{Z}}_t^l(u, v) = (\mathcal{R}_\phi^l \odot \mathcal{Z}_t^l(u, v)) \tag{6}$$

Lastly, the mixed tokens are transformed from the Fourier domain to the spatial domain with 2D IFFT \mathcal{F}^{-1} .

$$\tilde{u}_t^l(x, y) = \frac{1}{hw} \sum_{u=0}^{h-1} \sum_{v=0}^{w-1} \tilde{\mathcal{Z}}_t^l(u, v) e^{2\pi i (\frac{u}{h}x + \frac{v}{w}y)} \tag{7}$$

The general process of the Fourier block could be denoted as

$$\begin{aligned}
\tilde{u}_t^{F,l} &= \text{GELU}\left(u_t^{F,l} + \mathcal{F}^{-1}(\mathcal{R}_\phi^l \odot \mathcal{F}(u_t^{F,l}))\right), \\
u_t^{F,l+1} &= \left(\tilde{u}_t^{F,l} + \text{MLP}(\tilde{u}_t^{F,l})\right),
\end{aligned} \tag{8}$$

the residual connection and MLP are added to the Fourier layer to stabilize the training process. $u_t^{F,l}$ denotes the abbreviated version of $U_t^l(x, y)$.

Notably, inspired by recent advances in Fourier domain token mixers [27], [34], we directly use embedded patches from the encoder layer as the input of the Fourier-based residual module.

Adaptive Runge-Kutta Module (ARKM). To update the hidden state represented by the Transformer-based correction module and Fourier-based residual module in the PDE-guided way, we design the updating module with the adaptive second-

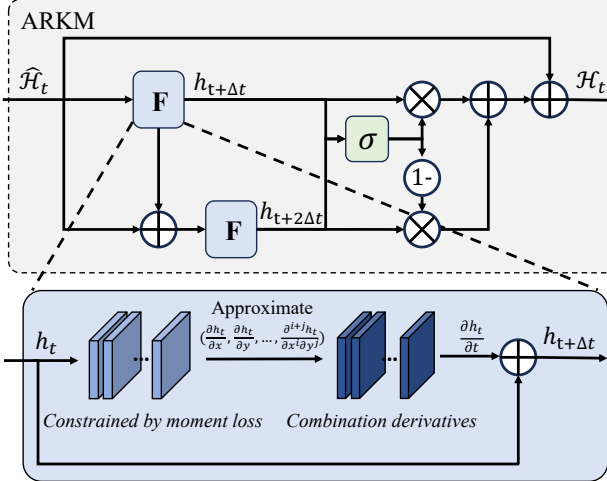


Fig. 4: The detailed structure of the adaptive second-order runge-kutta module. The input feature first computes derivatives utilizing the same differential approximator F and then updates with the gate mechanism.

order Runge-Kutta method to update the hidden states.

The Runge-Kutta methods are generally used in neural networks for updating, for example, the Euler method is the first-order version and could be regarded as residual connections. We first introduce the conventional second-order Runge-Kutta (RK2) method here, we have

$$\begin{aligned} h_{t+1} &= h_t + \frac{1}{2} (h_{t+\Delta t} + h_{t+2\Delta t}), \\ h_{t+\Delta t} &= F_\theta (h_t), \\ h_{t+2\Delta t} &= F_\theta (h_t + h_{t+\Delta t}), \end{aligned} \quad (9)$$

where $h_{t+\Delta t}, h_{t+2\Delta t}$ are assumed as the approximate solution at intermediate steps $t+\Delta t$ and $t+2\Delta t$ respectively and $\Delta t = 1/(\text{order}+1)$ in the Runge-Kutta method. Furthermore, the temporal derivative could be computed by combining spatial derivatives.

$$\frac{\partial h_t}{\partial t} = F_s \left(\frac{\partial h_t}{\partial x}, \frac{\partial h_t}{\partial y}, \frac{\partial^2 h_t}{\partial x \partial y}, \dots, \frac{\partial^{i+j} h_t}{\partial x^i \partial y^j} \right) \quad (10)$$

The function F_s is a combination of spatial partial derivatives.

Previous works generally directly utilize convolution to approximate the partial derivatives without any constraints. Although convolutional networks are capable of computing spatial derivatives, employing convolutions alone is not sufficient to illustrate the spatial partial derivatives are truly approximated. To force the convolution networks to calculate the spatial partial derivatives precisely and reasonably, we utilize the moment loss to constrain the computation weights of convolutions

Specifically, the procedure in Equation (10) could be separated as firstly utilizing a convolutional network $\text{Conv2d}_{k \times k}$ with k^2 kernels of size $k \times k$ to approximate the spatial derivatives $(\frac{\partial h_t}{\partial x}, \frac{\partial h_t}{\partial y}, \frac{\partial^2 h_t}{\partial x \partial y}, \dots, \frac{\partial^{i+j} h_t}{\partial x^i \partial y^j})$. Then utilizing another convolution network $\text{Conv2d}_{1 \times 1}$ with kernel size equal to 1×1 combines the spatial derivative into temporal derivatives. In this way, the temporal derivatives are precisely estimated.

However, we found that directly utilizing the conventional RK2 method may suffer gradient vanishes when the number of blocks is large. To solve the gradient vanishing problem, adapt the gate mechanism in the recurrent model, and improve the model performance, we design an adaptive RK2 method to scale the $h_{t+\Delta t}$ and $h_{t+2\Delta t}$ by learning the coefficients automatically in a data-driven way. Based on this idea, we utilize a weighted gate mechanism to scale the $h_{t+\Delta t}$ and $h_{t+2\Delta t}$. The procedure is denoted below:

$$\begin{aligned} \mathcal{H}_t &= \hat{H}_t + g \cdot h_{t+\Delta t} + (1-g) \cdot h_{t+2\Delta t} \\ g &= \text{sigmoid}(W_g * (h_{t+\Delta t}; h_{t+2\Delta t}) + b_g), \end{aligned} \quad (11)$$

where the weighted gate is computed by convolutions with 1×1 kernel W_g and bias b_g . \hat{H}_t is the sum of u_t^F and u_t^{TCM} . The architecture of the detailed structure is shown in Figure 4. It is worth noting that the function F_θ in the conventional RK2 method shared the same parameter θ in approximating $h_{t+\Delta t}$ and $h_{t+2\Delta t}$. We follow this setting in our module to reduce the constraints in the loss function. More details are shown in Section III-D.

Information Recalling Mechanism Last but not least, considering the information loss problem during the encoding procedure, we consider utilizing the information recalling mechanism between the encoder and decoder to enhance the model reconstruction ability. We separate the patch embedding layers into several sub-patch embedding layers. For example, if the patch size is 4×4 , we divide the patch embedding layers into two 2×2 convolution layers with kernel size and stride equal to 2. The same operation is utilized for patch reconstruction layers. In this way, the encoder and decoder could be denoted as

$$\hat{u}_t^l = \text{PatchInflated}_l (\hat{u}_t^{l-1} + u_t^{-l}), \quad l = 1, \dots, N. \quad (12)$$

Here, \hat{u}_t^l and u_t^{-l} represent decoded patches from the l^{th} layer of the decoder and the encoded patches from the l^{th} layer from the last layer of the encoder, respectively. PatchInflated_l denotes the l^{th} layer of the decoder with patch inflation operation.

C. Training Details

Models are trained utilizing the same training approaches. The details are in the Algorithm 1. There are two phases in training a recurrent model for spatiotemporal forecasting. During the first warm-up phase, the inputs of the model consist of the frames of the input sequence. During the second prediction phase, the output of the model from the previous time step is utilized as the input for the current time step. The loss function is computed by concatenating the outputs of the warm-up and prediction phase.

D. Loss Functions

In our experiments, we minimize the following loss to optimize our model:

$$\mathcal{L} = \mathcal{L}_{\text{prediction}} + \lambda_m \mathcal{L}_{\text{moment}}. \quad (13)$$

The prediction loss $\mathcal{L}_{\text{prediction}}$ contains two losses, the MSE loss and the H1 loss, which could be denoted as $\mathcal{L}^{MSE} + \lambda_H \mathcal{L}^{H1}$.

Algorithm 1 Training procedure

```

1: Require:  $\alpha$ , the learning rate.  $b$ , the batch size.  $n$ , the
   number of training epochs.  $T$ , the number of frames in
   the input sequence.  $T'$ , the number of frames in the target
   sequence.
2: Initialize parameters of network ( $\text{Net}_\theta$ ).
3: for  $i = 0, 1, \dots, n-1$  do
4:   for number of batches do
5:     Sample batch  $\{[x_{1:T}; y_{T+1:T+T'}]^{(j)}\}_{j=1}^b$ 
6:     Phase 1: Warm-up Phase
7:     Initialize  $\mathcal{H}_0, h_0, c_0$ 
8:     for  $t = 1, 2, \dots, T-1$  do
9:       Get  $\hat{x}_{t+1}, \mathcal{H}_t, h_t, c_t$ 
10:       $\text{Net}_\theta(x_t, \mathcal{H}_{t-1}, h_{t-1}, c_{t-1})$ 
11:    end for
12:    Phase 2: Prediction Phase
13:     $\hat{I}_0 \leftarrow x_T, \mathcal{H}_0 \leftarrow \mathcal{H}_{T-1}, h_0 \leftarrow h_{T-1}, c_0 \leftarrow c_{T-1}$ 
14:    for  $t = T, T+1, \dots, T+T'-1$  do
15:      Get  $\hat{x}_{t+1}, \mathcal{H}_t, h_t, c_t$ 
16:       $\text{Net}_\theta(\hat{x}_t, \mathcal{H}_{t-1}, h_{t-1}, c_{t-1})$ 
17:    end for
18:     $\mathcal{L} \leftarrow \mathcal{L}([\hat{x}_{1:T}; \hat{x}_{T+1:T+T'}], [x_{1:T}; y_{T+1:T+T'}])$ 
19:    Update  $\theta \leftarrow \theta - \alpha \nabla_\theta \mathcal{L}$ 
20:  end for
21: end for

```

In visual tasks, critical information is contained within the boundaries of objects or pixels with high contrast, corresponding to high-frequency information in the frequency domain. To enhance the model learn the high-frequency feature precisely, we introduce the frequency domain H1 loss to emphasize the high-frequency components in the image. The details of \mathcal{L}^{H^1} is

$$\mathcal{L}^{H^1}(\hat{\mathbf{x}}, \mathbf{y}) := \sqrt{\sum_{\xi=-N/2+1}^{N/2} (1 + 4\pi^2|\xi|^2) |\mathcal{F}(\hat{\mathbf{x}})_\xi - \mathcal{F}(\mathbf{y})_\xi|^2}. \quad (14)$$

In H1 loss, a term proportional to $|\xi|^2$ is introduced in the summation, where ξ denotes the frequency. By incorporating this term, the H1 loss can be interpreted as a weighted L2 loss emphasizing high-frequency components.

To force the convolution network in the Adaptive RK2 Module to approximate the spatial derivatives, we follow [16] to impose the moment loss $\mathcal{L}_{\text{moment}}$ to constrain the weights of the convolutions. Specifically, assuming a convolution network is parameterized by $\mathbf{w}_p = \{\mathbf{w}_{p,i,j}^k\}_{i,j \leq k}$ with k^2 filter of size $k \times k$. We aim to enforce each filter $\mathbf{w}_{p,i,j}^k$ to approximate the spatial derivative of order $(i, j) : \frac{\partial^{i+j} h}{\partial x^i \partial y^j}$ by using the moment loss. The calculation of the moment loss is derived from the filter as $\mathcal{M}(\mathbf{w}_{p,i,j}^k)$ and subsequently compared to the target moment matrix $M_{i,j}^k$ using the following equation.

$$\mathcal{L}_{\text{moment}}(\mathbf{w}_p) = \sum_{i \leq k} \sum_{j \leq k} \mathcal{L}^2(\mathcal{M}(\mathbf{w}_{p,i,j}^k), M_{i,j}^k) \quad (15)$$

where \mathcal{L}^2 is the squared error. More details are shown in the

next subsection.

E. Moment Matrix

In this work, we follow [16] to constrain convolutions to approximate partial derivatives. For a filter \mathbf{w} of size $k \times k$, the moment matrix $\mathcal{M}(\mathbf{w})$ is a matrix of size $k \times k$ defined as:

$$\mathcal{M}(\mathbf{w})_{i,j} = \frac{1}{i!j!} \sum_{u=-\frac{k-1}{2}}^{\frac{k-1}{2}} \sum_{v=-\frac{k-1}{2}}^{\frac{k-1}{2}} u^i v^j \mathbf{w}[u, v] \quad (16)$$

where $i, j = 0, \dots, k-1$.

For function $h : \mathbb{R}^2 \rightarrow \mathbb{R}$, we consider the convolution h with the filter \mathbf{w} . The Taylor expansion gives:

$$\begin{aligned} & \sum_{u=-\frac{k-1}{2}}^{\frac{k-1}{2}} \sum_{v=-\frac{k-1}{2}}^{\frac{k-1}{2}} \mathbf{w}[u, v] h(x + \delta x \cdot u, y + \delta y \cdot v) \\ &= \sum_{u=-\frac{k-1}{2}}^{\frac{k-1}{2}} \sum_{v=-\frac{k-1}{2}}^{\frac{k-1}{2}} \mathbf{w}[u, v] \sum_{i,j=1}^{k-1} \frac{\partial^{i+j} h}{\partial x^i \partial y^j}(x, y) \frac{u^i v^j}{i!j!} \delta x^i \delta y^j \\ &+ o(|\delta x|^{k-1} + |\delta y|^{k-1}) \\ &= \sum_{i,j=1}^{k-1} \mathbf{M}(\mathbf{w})_{i,j} \delta x^i \delta y^j \frac{\partial^{i+j} h}{\partial x^i \partial y^j}(x, y) + o(|\delta x|^{k+1} + |\delta y|^{k+1}) \end{aligned} \quad (17)$$

Therefore, the differential order approximated by the filter \mathbf{w} could be controlled by imposing constraints on its moment matrix $\mathcal{M}(\mathbf{w})$. To approximate the differential operator $\frac{\partial^{a+b}}{\partial x^a \partial y^b}$, the moment matrix should be imposed with $\mathcal{M}(\mathbf{w})_{i,j} = 0$ for $i \neq a$ and $j \neq b$. In this way, the target moment matrix $M_{i,j}^k$ of size $k \times k$ could be denoted as 1 at position (i, j) and 0 elsewhere. Thus, the moment loss could be denoted as Equation (15), which enforces each filter $\mathbf{w}_{p,i,j}^k$ to approximate the corresponding operator $\frac{\partial^{a+b}}{\partial x^a \partial y^b}$.

IV. EXPERIMENTS

We evaluate our proposed model on various benchmarks, including synthetic datasets, human video datasets, and natural scene datasets to evaluate the performance of our model. The details about the benchmarks are shown in Table I

A. Baselines

We compare our method with recent and advanced methods, including the and spatiotemporal and video prediction models.

- **Spatiotemporal Prediction Models:** We conduct experiments on advanced spatiotemporal prediction models. EarthFormer [36], Earthfarsser [23] and FNO [8].
- **Video Prediction Models:** We compare our method with recurrent-based ConvLSTM [9], PhyDNet [16], E3D-LSTM [10], SwinLSTM [20], CrevNet [11] and recurrent-free methods SimVP [4], Swin Transformer [6], Rainformer [37] and DMVFN [35] as the most advanced video prediction methods.

TABLE I: Details about the benchmark setting and model details. N_{train} and N_{test} denote the number of instances in the training and testing datasets. The length of the input and prediction sequence are T and T' , respectively. TB and FB denote the number of transformer blocks and Fourier blocks in training each dataset. Patch size and Dim are hyperparameters in each dataset.

BENCHMARKS	N_{train}	N_{test}	RESOLUTION	T	T'	TB	FB	PATCH SIZE	DIM
MOVING MNIST	10000	10000	(64,64,1)	10	10	6	8	(4, 4)	128
TAXIBJ	20461	500	(32,32,2)	4	4	6	8	(4, 4)	128
KTH	4940	3030	(128,128,1)	10	20	6	8	(4, 4)	128
SEVIR	6908	1392	(384,384,1)	10	10	8	10	(16, 16)	128
NAVIER-STOKES	1000	200	(64,64,1)	10	10	6	8	(4, 4)	64
WEATHER	2,167	706	(32,64,1)	12	12	6	8	(2,4)	128

TABLE II: Quantitative comparison of our method and other methods on **Moving MNIST**, **TaxiBJ** and **KTH**. Lower MSE, lower MAE, and higher SSIM indicate better predictions respectively. The number of parameters is counted when training the **Moving MNIST** dataset. The **Bold** and Underline denote the best and second best performance respectively.

Method	Parameters (M)	Moving MNIST			TaxiBJ			KTH		
		MSE ↓	MAE ↓	SSIM ↑	MAE ↓	SSIM ↑	MSE ↓	MAE ↓	SSIM ↑	
ConvLSTM [9]	15.0	29.80	90.64	0.9288	15.32	0.9836	47.65	445.50	0.8977	
PredRNN [12]	38.6	24.53	73.12	0.9462	15.37	0.9834	41.07	380.60	<u>0.9097</u>	
E3D-LSTM [10]	51.0	35.97	78.28	0.9320	15.26	0.9834	136.40	892.70	0.8153	
MAU [5]	4.5	26.86	78.22	0.9398	15.26	0.9834	51.02	471.20	0.8945	
CrevNet [11]	5.0	30.15	86.28	0.9350	15.73	0.9821	61.32	503.15	0.8815	
PhyDNet [16]	3.1	28.19	78.64	0.9374	15.53	0.9828	91.12	765.60	0.8322	
SwinLSTM [20]	20.1	27.74	77.21	0.9313	15.74	0.9813	45.23	437.51	0.9030	
DMVFN [35]	3.5	123.67	179.96	0.8140	15.72	0.9833	59.61	413.20	0.8976	
SimVP [4]	58.0	32.15	89.05	0.9268	15.45	0.9835	41.11	397.10	0.9065	
Ours	3.8	<u>24.83</u>	<u>74.83</u>	<u>0.9423</u>	14.88	0.9851	39.27	370.56	0.9173	
Ours(w/o H1)	3.8	25.19	75.74	0.9401	<u>14.96</u>	<u>0.9846</u>	<u>40.02</u>	<u>376.25</u>	0.9088	

B. Impletation

We use $L_{prediction} + L_{moment}$ loss for training all the datasets. The input and target frames of each dataset are normalized to the intensity of $[0, 1]$. Each model is optimized with the Adam optimizer and the model is trained on a single Nvidia 40G A100 GPU.

C. Evaluation metrics

We evaluate our model on three commonly used evaluation metrics, which include the Mean Squared Error (MSE) metric, the Mean Absolute Error (MAE), and the Structural Similarity Index Measure (SSIM). All metrics are averaged over prediction frames. Lower MAE and MSE or higher SSIM indicate better performance. In the SEVIR dataset, we utilize CSI-M as one of the evaluation metrics [36]. The CSI metric is commonly used in precipitation nowcasting, which is defined as

$$CSI = \frac{\#Hits}{\#Hits + \#Misses + \#F.Alarms}. \quad (18)$$

To count the #Hits (truth=1, pred=1), #Misses (truth=1, pred=1) and #F.Alarms (truth=0, pred=1), we follow the settings in [36] which rescale the prediction and the ground truth back to the range 0-255 and binarized at thresholds

(16, 74, 133, 160, 181, 219). The CSI-M denotes the mean value of various thresholds. In the Navier-Stokes dataset, we utilize N-MSE as the evaluation matrix [8], which is defined as

$$N\text{-MSE} = \frac{1}{B} \sum_{i=1}^B \frac{\|\hat{u}_i - u_i\|_2}{\|u_i\|_2} \quad (19)$$

where $\|\cdot\|_2$ is the 2-norm, B is the batch size, and \hat{u} is the prediction of the ground truth u .

D. Main Results

Moving MNIST. The moving MNIST [38] is the most widely used synthetic dataset. We follow the setting in OpenSTL [39] for generating the sequence with each sequence containing the first 10 frames for warm-up and the last 10 frames for prediction. In each frame, two handwritten digits move and bounce around in a 64×64 black canvas with fixed speed.

TaxiBJ. The TaxiBJ dataset [1] contains real-world taxi trajectory data collected in Beijing. The resolution of each frame is $32 \times 32 \times 2$, where the last dimension denotes the flow of traffic entering and leaving the same area with the temporal interval equals 30 minutes.

TABLE III: Quantitative comparison of our method and other methods on **SEVIR**, **Navier-Stokes** and **Weather** benchmarks. The single-variable temperature is forecasted in the WeatherBench. The number of parameters is counted when training in the weather dataset. * indicates that we rerun the official baselines in our experiment setting. Lower MSE, MAE, and N-MSE and higher CSI-M indicate better predictions. The **Bold** and Underline denote the best and second best performance respectively.

Method	Parameters (M)	SEVIR		Navier-Stokes		Weather	
		MSE $\times 100 \downarrow$	CSI-M $\times 100 \uparrow$	N-MSE $\times 100 \downarrow$	MSE \downarrow	MAE \downarrow	
ConvLSTM [9]	14.9	0.974	36.73	23.87	1.521	0.7949	
PredRNN [12]	23.6	0.621	41.13	19.53	1.331	0.7246	
MAU [5]	5.5	0.592	44.75	18.43	1.251	0.7036	
PhyDNet [16]	3.1	0.731	38.32	16.38	285.9	8.7370	
SimVP [4]	14.7	0.573	45.84	15.98	1.238	0.7037	
Swin Transformer [6]	12.4	1.012	34.11	18.63	1.143	<u>0.6735</u>	
Rainformer [37]	19.2	0.813	38.72	18.31	-	-	
EarthFormer* [36]	7.6	0.562	44.73	<u>15.39</u>	-	-	
Earthfarsser* [23]	21.3	<u>0.487</u>	<u>46.54</u>	15.64	<u>1.121</u>	0.6873	
FNO [8]	2.4	-	-	19.82	1.491	0.8130	
Ours	3.4	0.416	47.02	14.89	1.086	0.6226	

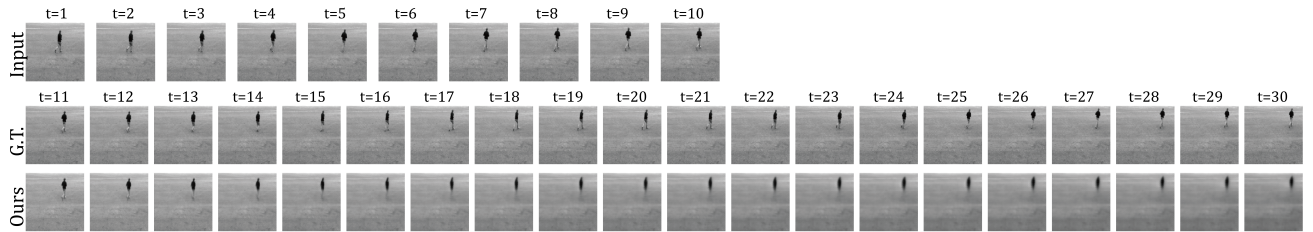


Fig. 5: Example of prediction results for the KTH dataset. Top: 1-10 time steps input sequence; Middle: 11-30 time steps ground truth sequence; Bottom: 11-30 time steps prediction sequence.

KTH. The KTH dataset [2] contains 25 individuals performing 6 types of human actions, including walking, jogging, running, boxing, hand waving, and hand clapping, in different 4 scenarios. We follow the setting in [39], the resolution of each frame is 128×128 and the prediction length is 20 in our experiments.

SEVIR. The SEVIR dataset [40] includes radar-based measurements of vertically integrated liquid (VIL), collected at 5-minute intervals with a spatial resolution of 1 km. The resolution of each frame is 384×384 . We follow the data preprocessing procedure of EarthFormer [36] and utilize the data of the year 2017 (29G) to train and test our model.

Navier-Stokes. The Navier-Stokes equation describes the vorticity forms on the two-dimensional torus \mathbb{T}^2 , which is a standard benchmark proposed in FNO [8]. Details of the equation are in the Appendix. Furthermore, as the Navier-Stokes equation is a standard benchmark for solving PDEs, we follow the baseline in [8] to utilize N-MSE for evaluation.

Weather. The Weather dataset [3] is an extensive weather prediction dataset that includes diverse climatic variables. The original data is transformed to a 5.625° resolution with a grid size of 32×64 points. The training, validation, and testing data are collected from 2010 to 2015, 2016 and 2017 to 2018 respectively. The time interval between each data point is one hour.

Results in Table II show that our model performs best in the

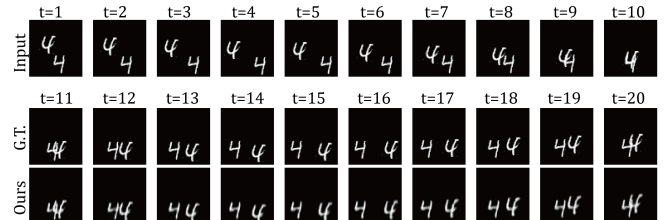


Fig. 6: Example of prediction results for the Moving MNIST dataset. Top: 1-10 time steps input sequence; Middle: 11-20 time steps ground truth sequence; Bottom: 11-20 time steps prediction sequence.

TaxiBj and KTH datasets and is second best in the Moving MNIST dataset. Notably, the number of parameters is much smaller than previous SOTA methods PredRNN [12], SimVP [4] and SwinLSTM [20]. Also, as shown in Table III, our model performs best in all the natural dynamic phenomena. Our model achieves the lowest MSE, MAE, and highest CSI-M on these datasets. Overall, our results illustrate the high efficacy of our model in precisely forecasting physical parameters and retaining structural details across diverse physical and video datasets, surpassing the performance of other state-of-the-art approaches.

We visualize the qualitative prediction results achieved by our model across multiple datasets, emphasizing its effective-

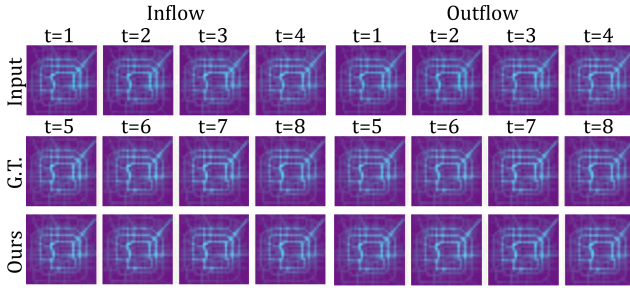


Fig. 7: Example of prediction results for the Moving TaxiBj dataset. Top: 1-4 time steps input sequence (there are two channels which denote as inflow and outflow respectively); Middle: 5-8 time steps ground truth sequence; Bottom: 5-8 time steps prediction sequence.

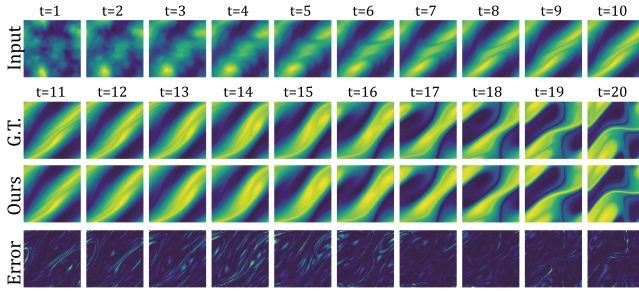


Fig. 8: Example of prediction results for the Navier-Stokes dataset. First row: 1-10 time steps input sequence; Second row: 11-20 time steps ground truth sequence; Third row: 11-20 time steps prediction sequence; Last row: 11-20 time steps absolute prediction error $|\hat{x} - y|$.

ness in precisely predicting future images. Our results illustrate our model accurately predicts human actions within KTH, as illustrated in Figure 5. Furthermore, Figure 6 and Figure 7 show that our model reliably predicts numerical motions within MovingMNIST and traffic flow changes in the TrafficBJ dataset. Last, our model performs well in the Navier-Stokes weather dataset, as shown in Figure 8, where it accurately predicts dynamic changes. Due to the computation source limitation, we do not visualize the results of other baselines. However, we find that visualizations of other baselines could be found in OpenSTL [39].

E. Ablation study

To verify the impact of each component within our model, we conduct ablation studies under different experimental conditions.

Patch size. The path embedding size directly influences the number of model parameters and the length of the input token sequence. A larger patch size produces a shorter token length. We conduct our ablation experiments on TaxiBj and KTH with patch size set to 2×2 , 4×4 , and 8×8 . Table IV shows that the optimal patch size may vary across datasets but the size of 4×4 generally works well.

The Decoder Layer. The decoder layer is to decode the hidden representation into the target output image. There are

TABLE IV: Ablation study on different patch sizes on TaxiBj and KTH benchmarks. The **Bold** denotes the best performance.

Patch size	TaxiBj		KTH	
	MAE \downarrow	SSIM \uparrow	MSE \downarrow	SSIM \uparrow
2	15.52	0.9839	43.16	0.9005
4	14.88	0.9851	40.17	0.9143
8	16.02	0.9818	53.98	0.8916

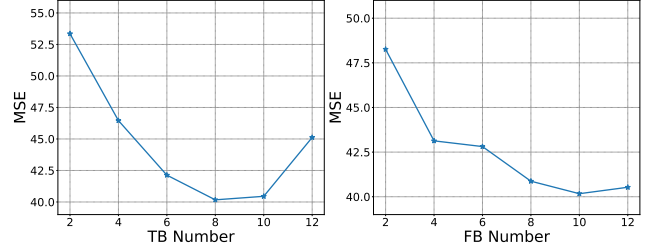


Fig. 9: Ablation study on the various numbers of Transformer Blocks (TB) and Fourier Blocks (FB) on KTH dataset.

many methods for upsampling the representations. Here, we design the experiments on two upsampling methods, ConvTransposed2D and Bilinear Interpolation, which are two commonly used vision tasks. Table V shows that the ConvTransposed2D method is much better than Bilinear Interpolation.

TABLE V: Ablation study on different upsampling methods in the Decoder layer on TaxiBj and KTH benchmarks. ConvT2D and Bi-Interp are the abbreviations of ConvTransposed2D and Bilinear Interpolation respectively. The **Bold** denotes the best performance.

Method	TaxiBj		KTH	
	MAE \downarrow	SSIM \uparrow	MSE \downarrow	SSIM \uparrow
ConvT2D	14.88	0.9851	40.17	0.9143
Bi-Interp	16.43	0.9637	50.36	0.8643

The number of Transformer and Fourier blocks. The number of blocks in each module highly influences the learning capacity of the model and the number of parameters. Owing to the limitation of computation resources, we fix the number of Transformer blocks to 8 or the number of Fourier blocks to 10 (the best setting in the KTH dataset) to explore the influence of the other blocks.

Also, to evaluate the effectiveness of the modules we proposed, we performed more ablation studies including removing components (w/o) and replacing them with other components (rep).

- In the *w/o* part, we consider removing Transformer Blocks (w/o TB), the Fourier-based Residual Modules (w/o FRM), the Adaptive RK2 Module (w/o ARKM), and the correction module (w/o CM).
- In the *rep* part, we consider replacing the Transformer Blocks with Feed Forward Networks (rep TB \rightarrow FFN), the Fourier Blocks with MLP (rep FB \rightarrow MLP), the Fourier-based Residual Module with UNet (rep FRM \rightarrow U-Net),

TABLE VI: Ablation studies on our proposed model, including *removing components (w/o)*, *replacing them with other components (rep)*. The **Bold** denotes the best performance.

DESIGNS		TAXIBJ		KTH	
		MAE↓	SSIM↑	MSE ↓	SSIM↑
W / O	TB	23.67	0.937	61.25	0.831
	FRM	20.36	0.951	52.15	0.872
	ARKM	16.73	0.972	45.67	0.898
	CM	15.06	0.973	43.04	0.903
R E P	TB→FFN	16.19	0.967	49.72	0.862
	FB→MLP	15.34	0.976	47.74	0.8719
	FRM→U-NET	14.97	0.984	40.42	0.908
	ARK2→EULER	15.24	0.980	42.01	0.908
ARK2→RK2		16.34	0.971	44.95	0.887
OURS		14.88	0.985	40.17	0.914

the Adaptive RK2 Method with Euler Method (rep ARK2→Euler), the Adaptive RK2 Method with conventional RK2 Method (rep ARK2→RK2).

The result shows that all components of our model are essential for spatiotemporal prediction after the removing (w/o) experiments. Especially, model performance will drop seriously without the Transformer Blocks and the Fourier-based module.

Similar results could be found in replacing experiments, the Transformer blocks and Fourier blocks are much better than FFN and MLP respectively. We reckon that this is because Transformer and Fourier layers have stronger abilities to model spatial correlations. Replacing the Fourier-based Residual Module with U-Net could obtain similar performance, but the number of parameters is much larger when using U-Net. Also, the Adaptive RK2 Module is much better than the conventional Euler, and the RK2 method with a slight increment in parameters is implemented. As the function to approximate partial derivatives in the update module is reusable, the higher-order methods will not significantly increase the number of parameters.

V. DISCUSSION AND CONCLUSION

The spatiotemporal prediction tasks have received wide attention recently. Many works have been proposed which utilize neural networks for weather forecasting. However, directly utilizing black-box networks could not get reliable prediction results. In this way, combining prior physical knowledge into neural networks is urgent to research to build human reliable neural networks. The physical knowledge, such as differential equations, and energy conservation laws, could help the neural networks to learn better physical reliable representations. In this way, more numerical analysis in the physical field could help to analyze the network features and representations. Also, with more natural environment data, many new kinds of research could be started to use neural networks to end scientific problems [41], [42].

In this paper, we propose a novel recurrent model that utilizes the Fourier blocks to enhance the spatiotemporal

representation learned by the Transformer blocks. Also, we combine frequency domain H1 loss with MSE loss to emphasize the boundary information in the frame. To approximate the physical state reasonably and accurately, we propose a new adaptive second-order Runge-Kutta module with physical-guided convolutions to update the state and calculate the partial derivatives. Our result shows that our model achieves superior performance in spatiotemporal and video prediction tasks with fewer parameter quantities.

REFERENCES

- [1] J. Zhang, Y. Zheng, and D. Qi, “Deep spatio-temporal residual networks for citywide crowd flows prediction,” in *Proceedings of the AAAI conference on artificial intelligence*, vol. 31, no. 1, 2017.
- [2] C. Schudt, I. Laptev, and B. Caputo, “Recognizing human actions: a local svm approach,” in *Proceedings of the 17th International Conference on Pattern Recognition, 2004. ICPR 2004.*, vol. 3. IEEE, 2004, pp. 32–36.
- [3] S. Rasp, P. D. Dueben, S. Scher, J. A. Weyn, S. Mouatadid, and N. Thuerey, “Weatherbench: a benchmark data set for data-driven weather forecasting,” *Journal of Advances in Modeling Earth Systems*, vol. 12, no. 11, p. e2020MS002203, 2020.
- [4] Z. Gao, C. Tan, L. Wu, and S. Z. Li, “Simvp: Simpler yet better video prediction,” in *Proceedings of the IEEE/CVF conference on computer vision and pattern recognition*, 2022, pp. 3170–3180.
- [5] Z. Chang, X. Zhang, S. Wang, S. Ma, Y. Ye, X. Xinguang, and W. Gao, “Mau: A motion-aware unit for video prediction and beyond,” *Advances in Neural Information Processing Systems*, vol. 34, pp. 26950–26962, 2021.
- [6] Z. Liu, J. Ning, Y. Cao, Y. Wei, Z. Zhang, S. Lin, and H. Hu, “Video swin transformer,” in *Proceedings of the IEEE/CVF conference on computer vision and pattern recognition*, 2022, pp. 3202–3211.
- [7] W. Yu, M. Luo, P. Zhou, C. Si, Y. Zhou, X. Wang, J. Feng, and S. Yan, “Metaformer is actually what you need for vision,” in *Proceedings of the IEEE/CVF conference on computer vision and pattern recognition*, 2022, pp. 10819–10829.
- [8] Z. Li, N. Kovachki, K. Azizzadenesheli, B. Liu, K. Bhattacharya, A. Stuart, and A. Anandkumar, “Fourier neural operator for parametric partial differential equations,” *arXiv preprint arXiv:2010.08895*, 2020.
- [9] X. Shi, Z. Chen, H. Wang, D.-Y. Yeung, W.-K. Wong, and W.-c. Woo, “Convolutional lstm network: A machine learning approach for precipitation nowcasting,” *Advances in neural information processing systems*, vol. 28, 2015.
- [10] Y. Wang, L. Jiang, M.-H. Yang, L.-J. Li, M. Long, and L. Fei-Fei, “Eidetic 3d lstm: A model for video prediction and beyond,” in *International conference on learning representations*, 2018.
- [11] W. Yu, Y. Lu, S. Easterbrook, and S. Fidler, “Efficient and information-preserving future frame prediction and beyond,” 2020.
- [12] Y. Wang, M. Long, J. Wang, Z. Gao, and P. S. Yu, “Predrnn: Recurrent neural networks for predictive learning using spatiotemporal lstms,” *Advances in neural information processing systems*, vol. 30, 2017.
- [13] Y. Wang, Z. Gao, M. Long, J. Wang, and S. Y. Philip, “Predrnn++: Towards a resolution of the deep-in-time dilemma in spatiotemporal predictive learning,” in *International conference on machine learning*, PMLR, 2018, pp. 5123–5132.
- [14] Y. Wang, H. Wu, J. Zhang, Z. Gao, J. Wang, S. Y. Philip, and M. Long, “Predrnn: A recurrent neural network for spatiotemporal predictive learning,” *IEEE Transactions on Pattern Analysis and Machine Intelligence*, vol. 45, no. 2, pp. 2208–2225, 2022.
- [15] W. Lotter, G. Kreiman, and D. Cox, “Deep predictive coding networks for video prediction and unsupervised learning,” *arXiv preprint arXiv:1605.08104*, 2016.
- [16] V. L. Guen and N. Thome, “Disentangling physical dynamics from unknown factors for unsupervised video prediction,” in *Proceedings of the IEEE/CVF Conference on Computer Vision and Pattern Recognition*, 2020, pp. 11474–11484.
- [17] J. Donà, J.-Y. Franceschi, S. Lamprier, and P. Gallinari, “Pde-driven spatiotemporal disentanglement,” *arXiv preprint arXiv:2008.01352*, 2020.
- [18] Y. Zhang, M. Long, K. Chen, L. Xing, R. Jin, M. I. Jordan, and J. Wang, “Skilful nowcasting of extreme precipitation with nowcastnet,” *Nature*, vol. 619, no. 7970, pp. 526–532, 2023.

[19] Y. Verma, M. Heinonen, and V. Garg, “Climode: Climate forecasting with physics-informed neural odes,” in *The Twelfth International Conference on Learning Representations*, 2023.

[20] S. Tang, C. Li, P. Zhang, and R. Tang, “Swinlstm: Improving spatiotemporal prediction accuracy using swin transformer and lstm,” in *Proceedings of the IEEE/CVF International Conference on Computer Vision*, 2023, pp. 13 470–13 479.

[21] G. Bertasius, H. Wang, and L. Torresani, “Is space-time attention all you need for video understanding?” in *ICML*, vol. 2, no. 3, 2021, p. 4.

[22] A. Arnab, M. Dehghani, G. Heigold, C. Sun, M. Lučić, and C. Schmid, “Vivit: A video vision transformer,” in *Proceedings of the IEEE/CVF international conference on computer vision*, 2021, pp. 6836–6846.

[23] H. Wu, S. Wang, Y. Liang, Z. Zhou, W. Huang, W. Xiong, and K. Wang, “Earthfarseer: Versatile spatio-temporal dynamical systems modeling in one model,” *arXiv preprint arXiv:2312.08403*, 2023.

[24] H. Wu, W. Xiong, F. Xu, X. Luo, C. Chen, X.-S. Hua, and H. Wang, “Pastnet: Introducing physical inductive biases for spatio-temporal video prediction,” *arXiv preprint arXiv:2305.11421*, 2023.

[25] X. Zhao, Y. Sun, T. Zhang, and B. Xu, “Local convolution enhanced global fourier neural operator for multiscale dynamic spaces prediction,” *arXiv preprint arXiv:2311.12902*, 2023.

[26] Z. Long, Y. Lu, X. Ma, and B. Dong, “Pde-net: Learning pdes from data,” in *International conference on machine learning*. PMLR, 2018, pp. 3208–3216.

[27] J. Guibas, M. Mardani, Z. Li, A. Tao, A. Anandkumar, and B. Catanzaro, “Adaptive fourier neural operators: Efficient token mixers for transformers,” *arXiv preprint arXiv:2111.13587*, 2021.

[28] T. Zhou, Z. Ma, Q. Wen, X. Wang, L. Sun, and R. Jin, “Fedformer: Frequency enhanced decomposed transformer for long-term series forecasting,” in *International Conference on Machine Learning*. PMLR, 2022, pp. 27 268–27 286.

[29] Y. Rao, W. Zhao, Z. Zhu, J. Zhou, and J. Lu, “Gfnet: Global filter networks for visual recognition,” *IEEE Transactions on Pattern Analysis and Machine Intelligence*, 2023.

[30] R. T. Chen, Y. Rubanova, J. Bettencourt, and D. K. Duvenaud, “Neural ordinary differential equations,” *Advances in neural information processing systems*, vol. 31, 2018.

[31] M. Raissi, P. Perdikaris, and G. E. Karniadakis, “Physics-informed neural networks: A deep learning framework for solving forward and inverse problems involving nonlinear partial differential equations,” *Journal of Computational physics*, vol. 378, pp. 686–707, 2019.

[32] X. Zhao, D. Zhang, H. Liyuan, T. Zhang, and B. Xu, “Ode-based recurrent model-free reinforcement learning for pomdps,” *Advances in Neural Information Processing Systems*, vol. 36, 2024.

[33] S. Park, K. Kim, J. Lee, J. Choo, J. Lee, S. Kim, and E. Choi, “Vid-ode: Continuous-time video generation with neural ordinary differential equation,” in *Proceedings of the AAAI Conference on Artificial Intelligence*, vol. 35, no. 3, 2021, pp. 2412–2422.

[34] Z. Qin, P. Zhang, F. Wu, and X. Li, “Feganet: Frequency channel attention networks,” in *Proceedings of the IEEE/CVF international conference on computer vision*, 2021, pp. 783–792.

[35] X. Hu, Z. Huang, A. Huang, J. Xu, and S. Zhou, “A dynamic multi-scale voxel flow network for video prediction,” in *Proceedings of the IEEE/CVF Conference on Computer Vision and Pattern Recognition*, 2023, pp. 6121–6131.

[36] Z. Gao, X. Shi, H. Wang, Y. Zhu, Y. B. Wang, M. Li, and D.-Y. Yeung, “Earthformer: Exploring space-time transformers for earth system forecasting,” *Advances in Neural Information Processing Systems*, vol. 35, pp. 25 390–25 403, 2022.

[37] C. Bai, F. Sun, J. Zhang, Y. Song, and S. Chen, “Rainformer: Features extraction balanced network for radar-based precipitation nowcasting,” *IEEE Geoscience and Remote Sensing Letters*, vol. 19, pp. 1–5, 2022.

[38] N. Srivastava, E. Mansimov, and R. Salakhudinov, “Unsupervised learning of video representations using lstms,” in *International conference on machine learning*. PMLR, 2015, pp. 843–852.

[39] C. Tan, S. Li, Z. Gao, W. Guan, Z. Wang, Z. Liu, L. Wu, and S. Z. Li, “Openstl: A comprehensive benchmark of spatio-temporal predictive learning,” *Advances in Neural Information Processing Systems*, vol. 36, 2024.

[40] M. Veillette, S. Samsi, and C. Mattioli, “Sevir: A storm event imagery dataset for deep learning applications in radar and satellite meteorology,” *Advances in Neural Information Processing Systems*, vol. 33, pp. 22 009–22 019, 2020.

[41] T. Zhang, X. Cheng, S. Jia, C. T. Li, M.-m. Poo, and B. Xu, “A brain-inspired algorithm that mitigates catastrophic forgetting of artificial and spiking neural networks with low computational cost,” *Science Advances*, vol. 9, no. 34, p. eadi2947, 2023.

[42] T. Zhang, X. Cheng, S. Jia, M.-m. Poo, Y. Zeng, and B. Xu, “Self-backpropagation of synaptic modifications elevates the efficiency of spiking and artificial neural networks,” *Science advances*, vol. 7, no. 43, p. eabh0146, 2021.